

Investigation of the temperature in dense carbon near the solid-liquid phase transition between 100 GPa and 200 GPa with spectrally resolved X-ray scattering

Helfrich, J.; Vorberger, J.; Frydrych, S.; Schaumann, G.; Gericke, D. O.; Ravasio, A.; Gauthier, M.; Fletcher, L. B.; Nagler, B.; Barbrel, B.; Bachmann, B.; Gamboa, E. J.; Göde, S.; Granados, E.; Lee, H. J.; Neumayer, P.; Schumaker, W.; Döppner, T.; Falcone, R. W.; Glenzer, S. H.; Roth, M.; Kraus, D.;

Originally published:

July 2019

High Energy Density Physics 32(2019), 56-62

DOI: <https://doi.org/10.1016/j.hedp.2019.05.001>

Perma-Link to Publication Repository of HZDR:

<https://www.hzdr.de/publications/Publ-26094>

Release of the secondary publication
on the basis of the German Copyright Law § 38 Section 4.

CC BY-NC-ND



LAWRENCE
LIVERMORE
NATIONAL
LABORATORY

Investigation of the Temperature in Dense Carbon near the Solid-liquid Phase Transition between 100 GPa and 200 GPa with Spectrally Resolved X-ray Scattering

J. Helfrich, J. Vorberger, S. Frydrych, G. Schaumann, D. O. Gericke, A. Ravasio, M. Gauthier, L. B. Fletcher, B. Nagler, B. Barbreil, B. Bachmann, E. J. Gamboa, S. Goede, E. Granados, H. J. Lee, P. Neumayer, W. Schumaker, T. Doeppner, R. W. Falcone, S. H. Glenzer, M. Roth, D. Kraus

October 4, 2017

High Energy Density Physics

Disclaimer

This document was prepared as an account of work sponsored by an agency of the United States government. Neither the United States government nor Lawrence Livermore National Security, LLC, nor any of their employees makes any warranty, expressed or implied, or assumes any legal liability or responsibility for the accuracy, completeness, or usefulness of any information, apparatus, product, or process disclosed, or represents that its use would not infringe privately owned rights. Reference herein to any specific commercial product, process, or service by trade name, trademark, manufacturer, or otherwise does not necessarily constitute or imply its endorsement, recommendation, or favoring by the United States government or Lawrence Livermore National Security, LLC. The views and opinions of authors expressed herein do not necessarily state or reflect those of the United States government or Lawrence Livermore National Security, LLC, and shall not be used for advertising or product endorsement purposes.

Investigation of the temperature in dense carbon near the solid-liquid phase transition between 100 GPa and 200 GPa with spectrally resolved X-ray scattering

J. Helfrich^a, J. Vorberger^b, S. Frydrych^a, G. Schaumann^a, A. Ravasio^c, M. Gauthier^c, L.B. Fletcher^c, B. Nagler^c, B. Barbreil^d, B. Bachmann^e, E.J. Gamboa^c, S. Göde^c, E. Granados^c, H.J. Lee^c, P. Neumayer^f, W. Schumaker^c, T. Döppner^e, R.W. Falcone^d, S.H. Glenzer^c, M. Roth^a, and D. Kraus^{b,d}

^a*Institut für Kernphysik, Technische Universität Darmstadt, Schlossgartenstraße 9, 64289 Darmstadt, Germany*

^b*Institute of Radiation Physics, Helmholtz-Zentrum Dresden-Rossendorf e.V. Bautzner Landstrasse 400, 01328 Dresden, Germany*

^c*SLAC National Accelerator Laboratory, Menlo Park, California 94309, USA.*

^d*Department of Physics, University of California, Berkeley, CA, United States*

^e*Lawrence Livermore National Laboratory, Livermore, California 94550, USA.*

^f*GSI Helmholtzzentrum für Schwerionenforschung GmbH, Planckstraße 1, 64291 Darmstadt, Germany.*

Abstract

We present experiments investigating dense carbon at pressures between 100 GPa and 200 GPa and temperatures between 5 000 K and 15,000 K. High-pressure samples with different temperatures were created by laser-driven shock compression of graphite and varying the initial density from 1.53 g/cm³ to 2.21 g/cm³ and the drive laser intensity from 7.1 TW/cm² to 14.2 TW/cm². In order to deduce temperatures, spectrally resolved X-ray scattering was applied to determine ion-ion structure factors at a scattering vector of $k = 4.12 \cdot 10^{10} \text{ m}^{-1}$, which shows high sensitivity to temperature for the investigated sample conditions. After comparison to corresponding DFT-MD simulations, we were able to assign each structure factor a temperature. This information is indicative of the expected temperature range for the melting line of carbon at high pressures and can be compared to theoretical predictions.

1. Introduction

The properties of carbon in the warm dense matter (WDM) regime play an important role in planetary physics and various experiments studying carbon under these extreme conditions have been performed in recent years. [1, 2, 3, 4, 5, 6, 7, 8, 9] following this motivation. These experiments include the investigation of liquid carbon and its possible influence on the magnetic moment of icy giant planets [10] or understanding the general processes in the high-pressure solid-liquid phase transition of carbon [11]. Inertial confinement fusion (ICF) is another important research area where properties of warm dense carbon play an important role. Here, carbon is present within plastic or diamond ablaters to drive the implosion of the fusion fuel by Newton's laws of motion. During compression process towards ignition, the ablator material passes through a broad regime of warm dense matter states [12, 13, 14].

Dynamic shock compression is a standard method to study materials in the high-pressure warm dense matter regime. Shock compression creates states of matter that are characterized by the Rankine-Hugoniot relations and the corresponding Hugoniot curve. Using sophisticated velocity, radiography, or diffraction measurements, it is possible to determine pressure and density for such states. Another important equation-of-state parameter, the temperature [15], is more difficult to obtain since typically, the samples last for only a few nanoseconds, their volume is small ($\approx (100 \mu\text{m})^3$) and generally opaque for optical light.

In this paper, we show a way to determine the temperature in

the final WDM state by measuring the ion-ion structure factor and compare it with density functional theory molecular dynamics (DFT-MD) simulations [16, 17]. We use spectrally resolved X-ray scattering from shock-compressed graphite samples applying ultrafast X-ray pulses of a few ten femtoseconds duration where the ratio of elastically and inelastically scattered radiation provides an absolute value of the ion-ion structure at a given scattering vector [16, 18]. By probing a regime that strongly changes from solid to liquid and at the same time is not affected by Bragg reflections of any possible solid phase [5, 19], we obtain a signal that is strongly sensitive to the temperature in the melting regime. In this way, using shock waves of around 10 km/s, we were able to access warm dense carbon states in the vicinity of the melting line in a pressure regime of 100 to 200 GPa.

2. Experiment Setup

The experiment was performed at the Matter in Extreme Conditions (MEC) instrument of the Linac Coherent Light Source (LCLS) based at SLAC National Accelerator Laboratory, USA. A sketch of the Experimental setup is shown in Fig. 1.

The laser pulses for compressing the graphite samples were focused onto the samples with a spot diameter of 150 μm at a wavelength of 527 nm and a pulse duration of 10 ns. Two different laser energy drive modes were applied: a "low drive" intensity of 7.1 TW/cm² (13 J per pulse) and a "high drive"

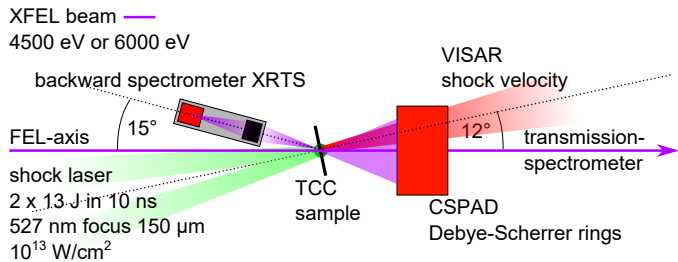


Figure 1: Sketch of the experimental setup. The FEL pulses are used to perform spectrally resolved X-ray scattering and diffraction measurements. The scattering spectrometer was placed in a backward scattering geometry and could scan scattering angles from 110 to 162 degrees in the experiment. In order to determine the shock transit time and with that the shock velocity, the reflectivity drop on the target rear side was recorded by a VISAR system. A large area pixel detector (CSPAD) was applied for the diffraction measurements. The samples were rotated by 12 degrees in respect to the FEL Beam to allow simultaneous VISAR measurements.

intensity of 14.2 TW/cm^2 (26 J per pulse). The surface irradiance was smoothed over the focal spot with hybrid random phase plates to achieve a reasonably planar and uniform shock drive into the approximately $80 \mu\text{m}$ thick samples. Each sample thickness had been characterized individually.

On the rear side, the targets were coated with an aluminum layer to increase the reflectivity for the VISAR system, to identify the interaction time of the X-ray beam with the target and to simplify the alignment of the XFEL beam. Due to the low Z-number of carbon an additional ablator material is not necessary for the experiment.

These carbon samples featured three different initial densities: 1.53 g/cm^3 , 1.84 g/cm^3 and 2.21 g/cm^3 , respectively. This corresponds to 67.7%, 81.4% and 97.8% of the density given by a perfect graphite lattice (2.26 g/cm^3). The two low-density graphites are made out of rigid graphite, which is produced from graphite powder under isostatic pressure and heat. The high-density samples consist of highly ordered Pyrolytic Graphite. This type of carbon has a purity of $> 99\%$, it is produced by splitting of hydrocarbon gas followed by a deposition process under low pressure and curing under several times atmospheric pressure [20].

The samples were probed with X-rays from the LCLS in SASE mode, focused down to 20 to $40 \mu\text{m}$ with photon energies of 4500 eV or 6000 eV. The ultra-short pulse durations (several ten's femtoseconds) allows for recording *in-situ* snapshots of the compression states.

For identifying the state of the shocked material in the P - ρ diagram, the shock-velocity and the density were determined directly for every driven sample. The moment of shock release was recorded by the velocity interferometer system for any reflector (VISAR), from which the shock transit time and subsequently the shock velocity were determined. The example illustrated in Fig. 2 shows a VISAR streak camera image recorded during the experiment. The image highlights the reflectivity loss during the interaction of the FEL pulse with the sample at 10.2 ns (blue), the shock breakout starting at 11.8 ns (green), and the bending of the breakout. The bending originates from the finite size of the laser spot and the three-dimensional spread

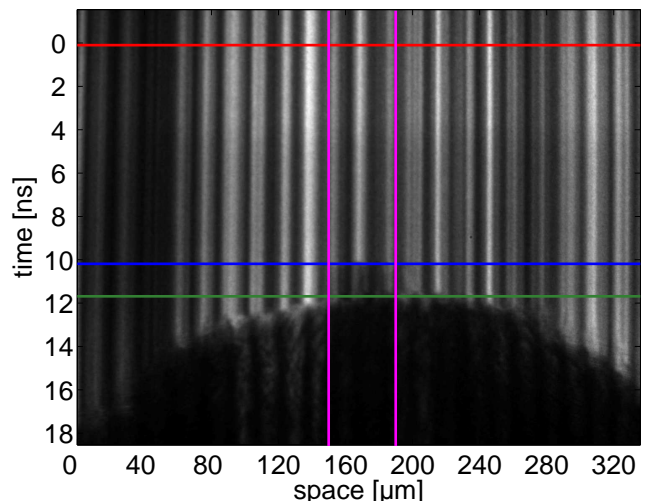


Figure 2: Example of the VISAR data. The red line marks the point where the laser pulse starts driving the shock wave and the green line marks the shock breakout. The curvature of the shock breakout in the VISAR image shows the spatial inhomogeneities of the shock wave due to the finite laser spot size (higher drive intensities in the center, lower drive intensities on the sides). The blue line marks the time when the FEL pulse interacts with the sample. Moreover, the spatial extend of the FEL pulse is recorded and shows that a region of reasonably constant shock transit time is probed in the experiment. The area between the purple lines marks the spatial extension of the XFEL spot.

of the shock wave inside the material. The temporal starting point of the drive laser is marked with 0 ns (red) and was previously determined by the VISAR system. Using the known temporal starting point of the laser light t_0 on the target front side and the shock breakout at the rear side, the error of the shock transit-time was determined to be smaller than 150 ps. The inaccuracy results from combining the uncertainty of t_0 , the streak delay and the measured breakout time. In combination with the known sample thickness, the shock velocity can be calculated for every measurement. The resulting error in the shock velocity for a single measurement is smaller than 0.2 km/s. We are confident that the probed sample volume is not influenced by side rarefactions since the central breakout regime is approximately planar. Moreover, additional VISAR measurements with a LiF window attached to the sample rear side show a graphite/LiF interface velocity that remains steady for several nanoseconds after the shock has traversed the graphite sample.

The density of the shocked material was determined by X-ray diffraction from cubic diamond structures which are formed during compression. These structures coexist for our conditions and do not completely vanish for the liquid case, and result in well defined diffraction signatures on the large area X-ray detector. Following Bragg's law, the diffraction angle α connected to the (111) crystal planes of diamond with a corresponding spacing of $d_{(111)}$ is given by

$$\sin \alpha = \frac{n\lambda}{2d_{(111)}}, \quad (1)$$

where λ is the chosen FEL wavelength and n is the diffraction order. The density ρ scales with $\rho \propto d_{(111)}^{-3}$ and thus, can easily be calculated for a known crystal structure.

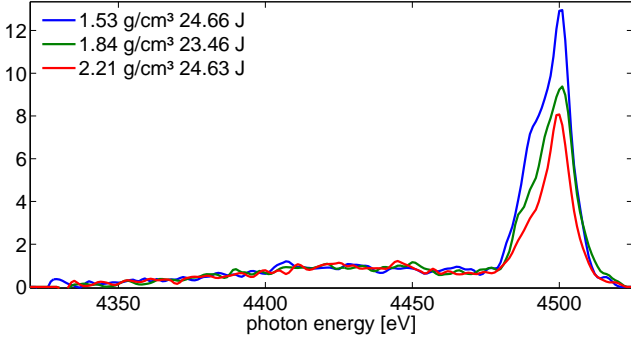


Figure 3: Spectrally resolved X-ray scattering results for shock-compressed graphite samples of different initial densities and a scattering vector of $k = 4.12 \cdot 10^{10} \text{ m}^{-1}$, driven with comparable laser energies, show a considerable difference in the elastic scattering strength. For better comparison, the spectra are normalized by the inelastic scattering feature.

Around 80 individual measurements were obtained for all of the three graphite types, where density and shock velocity could be extracted. The knowledge of the initial density ρ_0 , the density ρ_1 for the shocked sample and the shock velocity v_s allows for a determination of the corresponding pressure p_1 inside the sample by solving the Rankine-Hugoniot relations.

$$p_1 = v_s^2 \rho_0 \frac{\rho_1 - \rho_0}{\rho_1} \quad (2)$$

Applying these relations assumes a planar and steady shock. As the VISAR records a nearly planar shock release in the sample region that is probed by the X-rays (see Fig. 2), this assumption is justified.

In order to resolve absolute values of the ion structure, the backscattered radiation was recorded spectrally resolved. The crystal spectrometer was set up in a von Hamos geometry, used a HAPG crystal for spectral dispersion and a Cornell-SLAC Pixel Array Detector (CSPAD) for detecting the scattered X-rays [21]. The scattering angle was set to be 129° . Three examples of the recorded spectrally resolved scattering spectra are shown in Fig. 3. These measurements were performed for the three different graphite types with different initial density, all compressed by the "high drive" in this case. The difference in the elastic scattering amplitude is clearly visible. During the experiment, we probed the material just before the shock release. Measurements after this are dismissed since the sample conditions are no longer well-defined in the rarefaction induced by the shock breakout. For most of the samples, $\gtrsim 95\%$ of the material was shocked during the interaction time with the X-ray beam when the X-ray scattering data was taken.

3. Spectrally resolved X-ray scattering

In any given material, X-rays dominantly scatter from electrons. In our experiment the momentum transfer to the electron is small and the photon energy is nearly unchanged after the scattering process. This allows for approximating the scattering vector $k = k_i - k_s$, which is the difference between the incoming

wave vector k_i and the outgoing scattered wave vector k_s , with

$$k = |\mathbf{k}| = \frac{2\omega_i}{c_0} \sin(\theta/2) \quad (3)$$

where θ is the scattering angle and ω_i is the frequency of the incident light. In our experiment the scattering vector was $k = 4.12 \cdot 10^{10} \text{ m}^{-1}$.

The total scattered radiation per sample atom was calculated with the double-differential scattering cross section [22]

$$\frac{\partial^2 \sigma}{\partial \Omega \partial \omega} = \frac{r_0^2 \omega_s}{2 \omega_i} [1 + \cos^2 \theta] S(k, \omega), \quad (4)$$

where r_0 is the classical electron radius, ω_s the frequency of the scattered radiation, $\omega = \omega_i - \omega_s$ is the resulting frequency shift and $S(k, \omega)$ is the total electron structure factor, which includes all the microscopic information of the system. This behavior can be characterized in terms of the electron density fluctuations [23]

$$S(k, \omega) = \frac{1}{2\pi N} \int d\tau \langle \delta n_e(k, \tau) \delta n_e^*(k, 0) \rangle e^{i\omega\tau}, \quad (5)$$

with $n_e(k, \tau)$ denoting the Fourier transform of the electron number density fluctuation $\delta n_e(r, t)$ in space and N the number of sample atoms. In the warm dense matter regime, the effects from partial ionization and contributions from bound and free electrons must be considered. In partially ionized matter, Z_b electrons are still bound to the nucleus and Z_f electrons are free [23, 24]. The dynamic structure is then the sum of three scattering contributions: elastic scattering from electrons which are strongly bound to the core and from free electrons in the screening cloud around the cores (first term), inelastic scattering from free electrons (second term), and inelastic scattering from weakly bound electrons (third term) [26]

$$S(k, \omega) = |f(k) + q(k)|^2 S_{ii}(k, \omega) + Z_f S_{ee}(k, \omega) \quad (6)$$

$$+ Z_b \int S_{be}(k, \omega - \omega') S_s(k, \omega') d\omega'. \quad (7)$$

In this equation, $f(k)$ is the atomic form factor given by the bound electrons, $q(k)$ is the equivalent form factor of the free electron screening cloud surrounding the ions, $S_{ee}(k, \omega)$ is the dynamic structure factor of the free electrons, $S_{be}(k, \omega)$ describes the dynamic structure factor of the bound electrons, which must be convoluted with the self-motion of the ions, S_s contains the total dynamic contribution of the bound electrons. $S_{ii}(k, \omega)$ is the dynamic ionic structure factor and describes the correlation between the ions, which contains information about the ion structure.

In the regime of the solid-liquid phase transition, $S_{ii}(k, \omega)$ changes dramatically. The change comes from the amplitude dependence of the elastic scattering signal for a given scattering vector. The amplitude of the inelastic signal remains unchanged for all scattering vectors, since the electrons remain in covalent bonds upon melting, and can be used for normalization. For our experimental conditions and in non-collective scattering geometry, Eq. 7 can be simplified. Due to the low temperatures, there

is only a low degree of ionization and static ions. Consequently, there is a minor number of free electrons and the S_{ee} part does not lead to a significant contribution to the scattering signal and it can be neglected. The calculation of $q(k)$ in WDM is difficult, but for the chosen backscattering geometry, $q(k)$ is expected to be zero [25] and has no appreciable contribution. The last term of Eq. 7 contains the contributions from Raman scattering, which is typically very small in WDM [26, 27] and the scattering contributions from bound-free transitions from electrons in the K- and L-shell. In the case that free electrons can be neglected, the third term can be simplified to $\sum_{Z_{wb}}^{n=1} [1 - f_n(k)^2]$ [28]. With the assumption of static ions, the spectrally integrated scattering intensity at a certain wave number k is proportional to the static electron structure factor $S(k) = \int S(k, \omega) d\omega$. Under these conditions, we can write [26, 27, 28]

$$S(k) = |f(k)|^2 S_{ii}(k) + \sum_{Z_{wb}}^{n=1} [1 - f_n(k)^2]. \quad (8)$$

This equation separates the elastic scattering from tightly bound electrons in the first term and the scattering from Z_{wb} weakly bound electrons with the corresponding single-electron form factors $f_n(k)$ which can be calculated by the use of hydrogenic wave functions [29]. With the known form factors, the static ion structure factor can be determined by a measurement of the ratio between the intensities of the elastic and the inelastic scattering signal [30, 5, 31]:

$$S_{ii}(k) = \frac{1}{|f(k)|^2} \left[\sum_{Z_{wb}}^{n=1} [1 - f_n^2(k)] \right] \frac{x_{el}}{x_{inel}}. \quad (9)$$

x_{el} is the intensity of elastic scattering and x_{inel} is the intensity of inelastic scattering. The major benefit of measuring $S_{ii}(k)$ in this way is, that there is no need of an absolutely calibrated detector, because only the ratio between the scattering signal is needed. For the chosen wave vector $k = 4.12 \cdot 10^{10} \text{ m}^{-1}$, which is probed in our experiment, S_{ii} is expected to be small for the solid material and shows a continuous increase up to $S_{ii} \approx 1$ which is comparable to temperatures of about 15,000 K.

4. Simulations

The density functional molecular dynamics (DFT-MD) simulations have been performed using the code VASP [32, 33, 34, 35]. We used supercells with periodic boundary conditions containing $N = 192$ or $N = 216$ carbon nuclei, depending on the initial conditions. The time step for the molecular dynamics of the ions was $\delta t = 0.192 \text{ fs}$. The ion temperature was controlled using a Nose-Hoover thermostat [36]. The electrons were described using the Mermin functional with Fermi-smearing at the appropriate temperature of the electrons. Exchange and correlation contributions were taken into account by means of the GGA-PBE functional [37, 38]. The electron-ion interaction uses a pseudopotential within the PAW method [39, 40].

The four $2s$ and $2p$ electrons are considered to be valence electrons, the $1s$ electrons are treated as core electrons and

taken explicitly into account. The core radius is $r_c = 1.5a_B$. The electronic wave function was expanded into plane waves with an energy cutoff of $E_{cut} = 900 \text{ eV}$. The warm dense matter conditions considered demanded that the number of bands be increased up to 900 for the highest temperatures considered. We performed two series of DFT-MD simulations. The first series starts with a diamond lattice at a low temperature where carbon is a solid. Successive runs at increasing temperatures use as initial state converged and equilibrated snapshots from a run at slightly lower temperature, starting at $T = 4,000 \text{ K}$. The second series of simulations starts in the fluid at $T = 3 \text{ eV}$ and further runs simulating the fluid at lower temperatures take initial conditions from snapshots at slightly higher temperatures.

The liquid phase of carbon features short-lived chemical bonds [41] and Fig. 4 shows the influence of the temperature on the results of the DFT-MD simulations for the structure factor. The simulations show the strong change of the structure factor between $3.5 \cdot 10^{10} \text{ m}^{-1}$ and $4.5 \cdot 10^{10} \text{ m}^{-1}$ for temperatures up to 15 000 K. For higher temperatures, the change in the structure factor is small and the factor is unity one for higher temperatures. At 10 000 K, the bonds in the complex carbon liquid are starting to dissolve and the carbon builds a single atom liquid. Another observation in Fig. 4 is that a structure factor above 0.8 indicates a liquid state. In order to distinguish between the solid and liquid state, we evaluated the diffusion (mean square displacement) of the atoms for each simulation.

The resulting structure factor will also depend on the density of the sample. The influence is shown in Fig. 5 and shows a shift of the curve to higher scattering vectors for higher densities [42]. The change of the structure factor due to the uncertainty in the density, is of subordinate role compared to the change of the structure factor for different temperatures.

5. Results

Our results for the averaged shock velocity of the different graphite samples are shown in Table 1. The results show very similar shock velocities with slightly higher values for the low density samples. The errors contain the temporal jitter of the streak cameras and the laser system.

Figure 6 contains parts from the measured Debye-Scherrer-Rings for the density determination. The data originate from a sample with an initial density of 1.84 g/cm^3 for the unshocked material, the same sample shocked with 7.1 TW/cm^2 (low intensity) and a sample of the same type shocked with 14.2 TW/cm^2 (high intensity).

The discussed measurements were taken when the shock-wave passed 98% of the target in the propagation direction for the low intensity run and 95% using high intensity. This values were determined by the reflection change on the target rear side (compare Figure 2).

We clearly observe a strong reduction of the graphite (002) peak for the shocked material. The remaining graphite scattering signals are due to unshocked graphite in the scattering volume. Additionally, we can see the aluminum scattering signal from the reflectivity coating for VISAR. At 63.5° (low intensity) and 64.1° (high intensity), we observe the formation of a

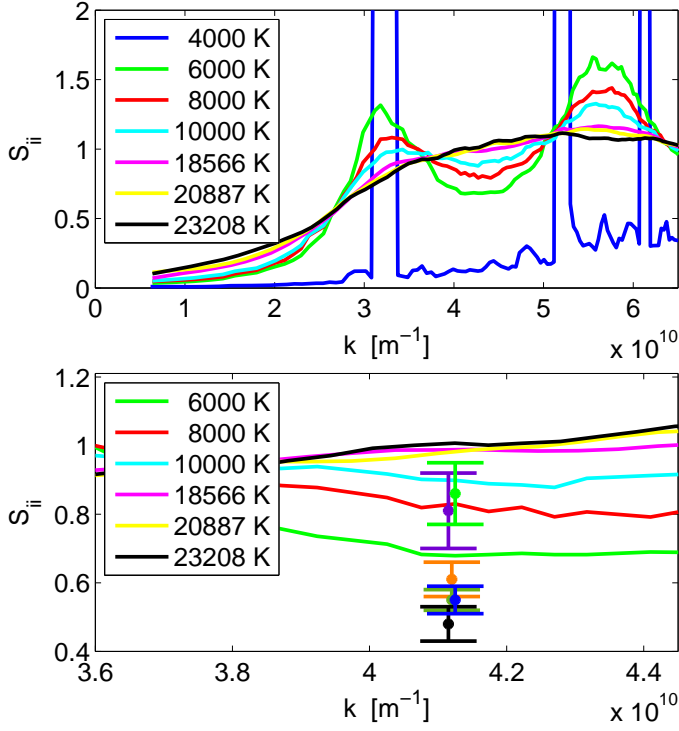


Figure 4: The top panel shows the influence of temperature on the behaviour of the structure factor. In the fluid at lower temperatures, we observe two correlation peaks at $3.2 \cdot 10^{10} \text{ m}^{-1}$ and $5.8 \cdot 10^{10} \text{ m}^{-1}$. These peaks are in the proximity of the Bragg-Peaks from graphite with a density of 4.00 g/cm^3 . The blue simulation at 4000 K is a cubic diamond structure. All simulations with a temperature of 10000 K and above were started in the fluid phase. The simulations for 6000 K and 8000 K started in the solid (diamond) phase. The bottom panel shows the results from our measurements. (purple 1.53 g/cm^3 high intensity, green 1.53 g/cm^3 low intensity, orange 1.84 g/cm^3 high intensity, dark green 1.84 g/cm^3 low intensity, blue 2.21 g/cm^3 high intensity, black 2.21 g/cm^3 low intensity)

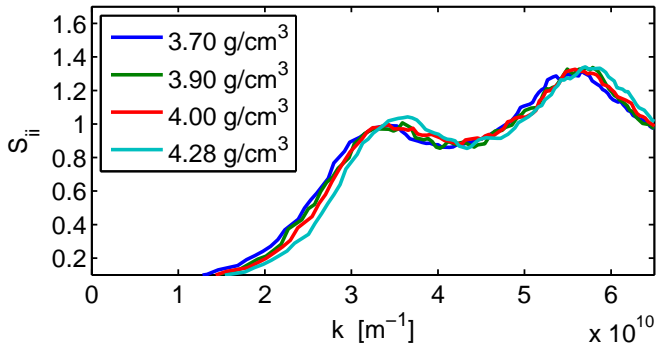


Figure 5: The influence of the density applied in the simulations on the results of the structure factor for liquid carbon at 10000 K . For higher densities, the resulting structure factor curve shifts to higher scattering vector values.

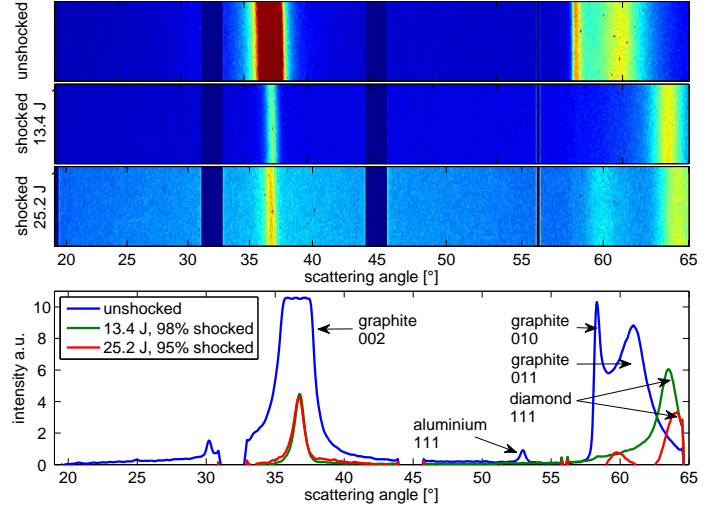


Figure 6: The measurements show the resulting diffraction signals for a sample with an initial density of 1.84 g/cm^3 . The first bar in the upper picture corresponds to an unshocked sample with the signals from the graphite (002), (010) and (011) planes. In the middle, the same sample compressed with a laser intensity of 7.1 TW/cm^2 (13.4 J) is shown and the third bar relates to a sample compressed with an intensity of 14.2 TW/cm^2 (25.2 J).

low energy 7.1 TW/cm^2	shock velocity km/s	density g/cm^3	pressure GPa
1.53 g/cm^3	10.5 ± 1.5	3.82 ± 0.21	102 ± 31
1.84 g/cm^3	10.1 ± 1.3	3.87 ± 0.16	100 ± 26
2.21 g/cm^3	10.0 ± 1.5	3.87 ± 0.22	97 ± 28
high energy 14.2 TW/cm^2	shock velocity km/s	density g/cm^3	pressure GPa
1.53 g/cm^3	13.4 ± 0.6	4.16 ± 0.22	174 ± 18
1.84 g/cm^3	12.8 ± 0.7	4.24 ± 0.12	172 ± 24
2.21 g/cm^3	12.7 ± 0.7	4.18 ± 0.13	168 ± 20

Table 1: Measured shock velocities and densities averaged over all measurements and the resulting pressures inside the sample, calculated with Eq. 2. The table includes the data for all initial densities for low and high laser intensities.

cubic diamond structure. The diamond peaks correspond to the (111) planes and we can calculate the density in the compressed material using Eq. (1). For the shown examples, Eq. (1) results in densities of $4.03 \pm 0.12 \text{ g/cm}^3$ (63.5°) and $4.16 \pm 0.12 \text{ g/cm}^3$ (64.1°). If we compare the diamond signal strength of these examples, we find that for the high laser intensity, the signal is weaker than for the low intensity drive. This is an effect of the phase transition during the shock process, where some graphite grains partly transform to diamond before the transition to the liquid is completed. For higher shock velocities, the number of the remaining structures inside the sample is smaller than for lower shock velocities. The averaged final densities for the different laser intensities and sample densities are given in Table 1 which also includes the resulting pressures calculated with Eq. (2) and the measured shock velocities. With this, we are able to define the position in the $P - \rho$ phase diagram for all measurements.

For the investigation of the material phase and the temperature, we analyzed the ion-ion-structure factor data. An example

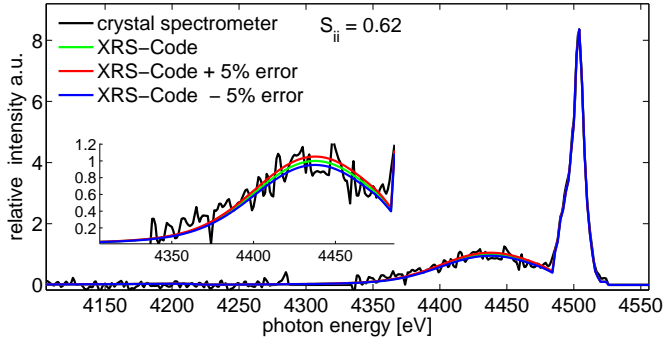


Figure 7: X-ray scattering spectrum taken with the backward spectrometer from shocked graphite (2.21 g/cm^3 and high intensity) together with the calculated spectrum from the elastic scattering signal (detector gap between -216 eV and -170 eV). The inset shows the zoomed inelastic scattering signal.

of the data from the backward spectrometer with the XRTS data is depicted in Fig. 7. The measurement shows the inelastic and elastic scattering signal, which are represented by x_{inel} and x_{el} in Eq. (9). The shape of the elastic feature corresponds to the FEL input spectrum.

To determine the ion-ion-structure factor we used the X-Ray Scattering (XRS) Code (version 6.1.0) originally developed by G. Gregori et al. [26, 27]. An example of the code results and a corresponding measurement is shown in Fig. 7. The uncertainty of this calculation is assumed with a $\pm 5\%$ error. This error results from the determination of the intensity ratio of the elastic to the inelastic scattering signal.

For obtaining information on the P - ρ phase diagram, we used the structure factor as a third dimension and compare the three different initial densities. These results are shown in Fig. 8. We compare our measurements in the phase diagram with measurements performed by W.H. Gust [43] and M. van Thiel [44]. The results are in good agreement and provide higher pressures and densities for the three initial densities. The measurements of W. H. Gust were performed for initial densities of 1.54 g/cm^3 , 1.70 g/cm^3 and 2.20 g/cm^3 and of M. van Thiel for 1.54 g/cm^3 , 1.75 g/cm^3 and 2.20 g/cm^3 . In accordance with Fig. 4, a higher structure factor at this scattering vector indicates a higher temperature.

In the next step, we relate every measured structure factor with a temperature, using the DFT-MD simulations. One result from the DFT-MD simulations is that a structure factor $S_{ii} > 0.8$ for $k = 4.12 \cdot 10^{10} \text{ m}^{-1}$ indicates a liquid (see Fig. 4) and that all measurements with a structure factor above this value are indicating pure liquid carbon. For an accurate analysis, the density must be taken into account for the temperature determination. Fig. 5 shows the density dependence of the structure factor and the shift of the curve to higher values for higher densities. In our density regime between 3.7 g/cm^3 and 4.3 g/cm^3 the curve shifts nearly linearly, and for our density corrections for S_{ii} we assume the shift to be linear. For the final temperature assessment, the structure factor curve has been shifted in accordance with the density for each measurement and analyzed for the chosen scattering vector. The temperature for the measured ion-ion-structure factors is linearly interpo-

lated between the individual DFT-MD simulations results. For lower temperatures than 6000 K , the simulations show a solid structure and the ion-ion-structure factor is orders of magnitude smaller than the peak intensities at the Bragg reflections. To obtain approximate temperatures for the intermediate regime, we linearly interpolated between the simulations for $6,000 \text{ K}$ and $3,900 \text{ K}$. The assumption of a linear interpolation may add an additional systematic uncertainty for the extracted temperatures from the corresponding scattering data resulting in ion-ion structure values in this regime. For temperatures smaller than 3900 K , we use the Debye-Waller factor to compute the diffuse scattering between Bragg peaks from the solid phase. The Debye temperatures needed as input were obtained from DFT-MD. For different Debye Temperatures between 2000 K and 6000 K we get an averaged ion-ion-structure factor $S_{ii} = 0.07$ for $k = 4.12 \cdot 10^{10} \text{ m}^{-1}$.

The situation inside the shocked material after the shock process can be described as a liquid which includes solid structures. While the ratio of solid structures to liquid material depends on the strength of the shock and the initial density of the carbon sample. The composition of the sample ranges from a liquid coexisting with some small solid structures to a sample with compounded. In the case of remaining structures for conditions below the transformation of the solid carbon to the liquid state, the temperature is not well defined with this method. But the method gives a temperature for the liquid part of the material in this shock induced transition process.

The temperatures resulting from the measurements illustrated in Fig. 8 are shown in Fig. 9 and compared with results from previous experiments [31] and with several predictions of the carbon solid-liquid phase transition. Of these results, models relying on DFT-MD to extract free energy surfaces in order to determine the melt line are broadly in agreement with our results [11, 47, 48, 49, 50]. However, more approximate models using effective potentials or given functional shapes of the equation of state (using free parameters) are not consistent with our findings [51, 52, 53, 54]. In this paper, we use DFT-MD to investigate the microscopic structure and to circumvent the need to calculate the entropy by developing a model for the solid to liquid transition based on the static structure factor.

In the investigated temperature and pressure regime, we expect a melt line with a positive slope. With a start point around 6000 K at 100 GPa and an endpoint around 8000 K at 200 GPa .

6. Conclusions

Using laser-driven shock-compression in combination with spectrally resolved X-ray scattering, we were able to determine approximate temperature values via the ion structure factor in addition to density and pressure of the shocked carbon samples. Laser intensities of 7.1 TW/cm^2 and resulting shock velocities of 10 km/s are not high enough to reach a pure liquid carbon sample for initial density $1.53 \text{ g/cm}^3 < \rho < 2.21 \text{ g/cm}^3$. With these laser intensities, our final conditions for the shocked material are very similar and we have reached relatively constant pressures of 100 GPa and final densities of 3.85 g/cm^3 .

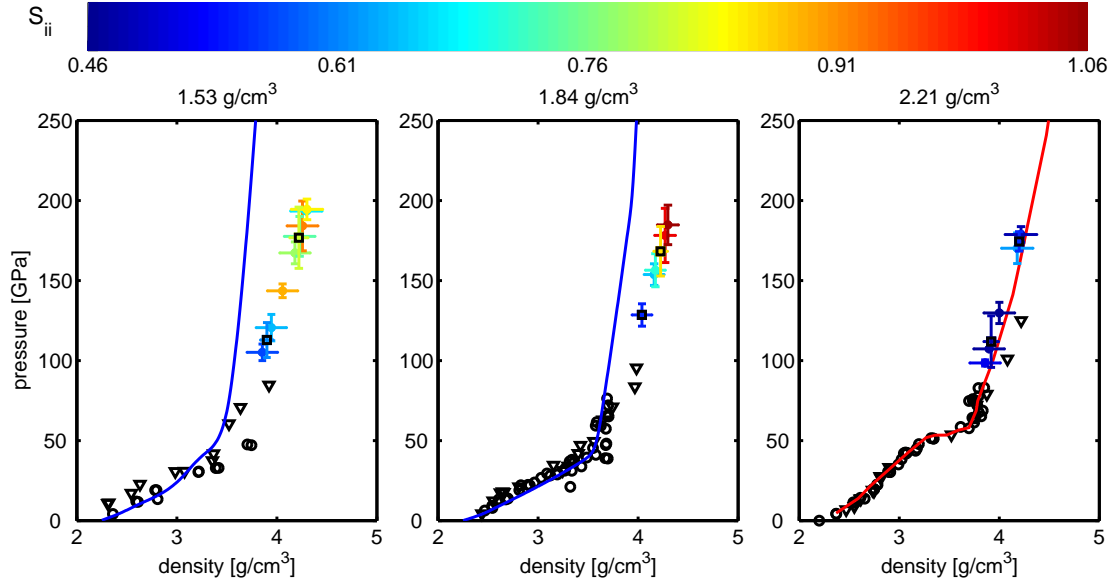


Figure 8: The graphics shows our measurements compared with the results from M. van Thiel [44] (black rings) and W.H. Gust [43] (black triangles) for the three different graphite types with their measurements for pressures up to 100 GPa. The rectangles with corresponding errorbars shows our results in the P- ρ phase diagram with pressures up to 200 GPa. The color map shows the resulting structure factor for the measurements and the black rectangle marks the averaged values for low and high laser intensities. For 2.21 g/cm³, we can compare our data with a common Hugoniot curve that is benchmarked by experiments to pressures up to 760 GPa by W.J. Nellis et al. [45] (red line) and shows excellent agreement with our data. For 1.53 g/cm³ and 1.84 g/cm³, there does not exist comparable data and a comparison to Hugoniot curves extracted from SESAME table 7832 (blue lines) [46], which is constructed for porous carbon and is only benchmarked at lower pressures than achieved in our experiment, results in poor agreement at high pressures.

density ρ_0 [g/cm ³]	shock velocity v_s [km/s]	density ρ_1 [g/cm ³]	pressure p_1 [GPa]	S_{ii}	temperature [K]
1.53	11.0±0.5	3.90 ±0.06	113 ±11	0.61 ±0.05	5 700 ⁺¹⁰⁰ ₋₁₀₀
1.84	11.3± 0.2†	4.04±0.10†	129 ±7†	0.55 ±0.03†	5 600 ⁺¹⁰⁰ ₋₁₀₀
2.21	10.7±0.6	3.92 ±0.07	112 ±16	0.48 ±0.05	5 300 ⁺¹⁰⁰ ₋₁₀₀
1.53	13.4± 0.7	4.22 ±0.09	177 ±19	0.81 ±0.11	7 800 ⁺³¹⁰⁰ ₋₁₆₀₀
1.84	12.7± 0.5	4.23 ±0.07	168 ±16	0.86 ±0.09	9 200 ⁺⁵⁷⁰⁰ ₋₁₉₀₀
2.21	12.9± 0.2	4.20 ±0.03	175 ± 6	0.55 ±0.04	5 600 ⁺¹⁰⁰ ₋₁₀₀

Table 2: The tabular shows the averaged results for all measurements with the scattering vector $k = 4.12 \cdot 10^{10} \text{ m}^{-1}$ for the three initial carbon densities, depending on the shock velocity v_s († only one measurement, error single measurement).

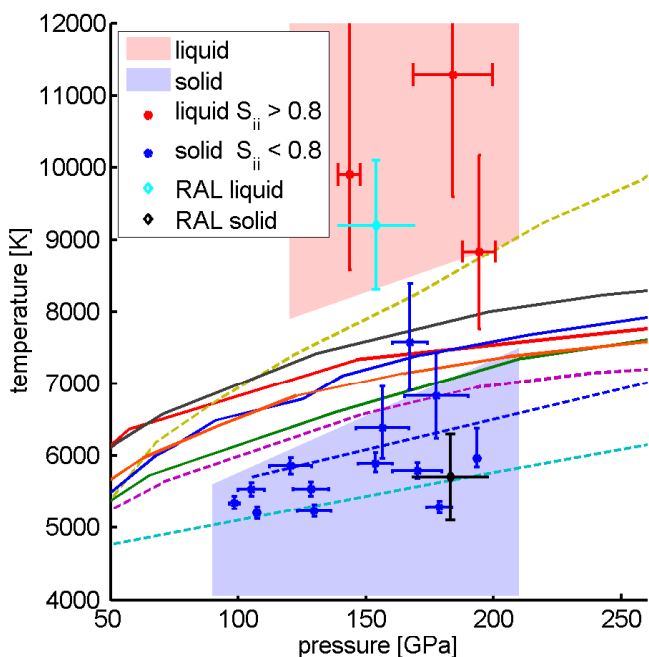


Figure 9: Comparison of our results with different simulations for the phase transition for carbon from the solid to the liquid state. The red marks shows measurements which were identified as liquid. The blue signs are shocked samples which remain solid or in a coexistence state whose structure factor does not fit into a pure liquid sample. With this information, we marked two areas, one in red (pure liquid) and a blue area (solid). The RAL diamond symbols show some results from earlier experiments [31]. The theoretical melting curves drawn as solid lines are consistent with our results (black solid X. Wang [47], green solid F. P. Bundy [48], red solid M. P. Grumbach [50], blue solid A. A. Correa [49], orange solid L. Benedict [11]). Dashed lines are used for theoretical predictions that are not consistent to our results (Blue dash M. van Thiel[51], turquoise dash A. M. Molodets [52], purple dash L. E. Fried [53], yellow dash L. M. Ghiringhelli [54]).

For laser intensities of 14.2 TW/cm^2 , we observe shock velocities of 13 km/s , resulting in pressures of 170 GPa and densities of 4.20 g/cm^3 . The x-ray diffraction signals show us the disappearing of the graphite structure and the forming of some cubic diamond structures which can be used for density determination. The XRTS scattering allows absolute calibration of the signals to give the ion-ion-structure factor for the shocked samples. In combination with DFT-MD simulations, this allows conclusions as to the temperature and the phase state in the shocked material. Finally, a comparison of the data for the solid diamond and liquid carbon phase to predictions from a variety of theories is performed. Although several models predict melting lines inconsistent with our results, while others seem in reasonable agreement, the achieved accuracy is not yet sufficient to provide an accurate measurement of the melting line. Future work on combination of DFT-MD and x-ray scattering experiments will aim to enhance the accuracy.

Acknowledgments

We thank the staff scientists, and laser technicians of the MEC at LCLS for their assistance and motivation. We further appreciate the work done by the target laboratory of the TU Darmstadt and the GSI for the target manufacture. Use of the Linac Coherent Light Source (LCLS), SLAC National Accelerator Laboratory, is supported by the U.S. Department of Energy, Office of Science, Office of Basic Energy Sciences under Contract No. DE-AC02-76SF00515. This work was performed at the Matter at Extreme Conditions (MEC) instrument of LCLS, supported by the US Department of Energy Office of Science, Fusion Energy Science under contract No. SF00515. D.K., B. Barbrel and R.W.F. acknowledge support by the US Department of Energy, Office of Science, Fusion Energy Sciences and by the National Nuclear Security Administration under Award Numbers DE-FG52-10NA29649 and DENA0001859. SLAC HED is supported by DOE Office of Science, Fusion Energy Science under FWP 100182. J.H., S.F. and M.R. were supported by German Bundesministerium für Bildung und Forschung project Nos. 05P12RDF A1 and 06DA9043I. D.K. was supported by the Helmholtz Association under VH-NG-1141. The work of B. Bachmann and T.D. was performed under the auspices of the US Department of Energy by Lawrence Livermore National Laboratory under Contract No. DE-AC52-07NA27344.

- [1] D. Batani, F. Strati, H. Stabile, M. Tomasini, G. Lucchini, A. Ravasio, M. Koenig, A. Benuzzi-Mounaux, H. Nishimura, Y. Ochi et al., Phys. Rev. Lett. 92, 065503 (2004).
- [2] M. D. Knudson et al., Science 322, 1822 (2008).
- [3] J. H. Eggert et al., Nature Physics, 6, 4043 (2009).
- [4] A. Pelka et al., Phys. Rev. Lett. 105, 265701 (2010).
- [5] D. Kraus et al., Phys. Rev. Lett. 111, 255501 (2013).
- [6] R. F. Smith et al., Nature 511 (7509), 330 (2014).
- [7] D. Kraus et al., Nature Communications 7, 10970 (2016).
- [8] D. Kraus et al., Nat. Astron. 1, 606-611 (2017).
- [9] N. J. Hartley et al., Phys. Rev. Lett. 121, 245501 (2018).
- [10] S. Stanley and J. Bloxham, Nature 428, 151 (2004).
- [11] L. X. Benedict, K. P. Driver, S. Hamel, B. Militzer, T. Qi, A. A. Correa, A. Saul, and E. Schwegler, Phys. Rev. B 89, 224109 (2014).

- [12] J. D. Lindl, P. Amendt, R. L. Berger, S.G. Glendinning, S. H. Glenzer, S.W. Haan, R. L. Kauffman, O. L. Landen, and L. J. Suter, *Phys. Plasmas* 11, 339 (2004).
- [13] A. J. MacKinnon, et al., *Phys. Plasmas* 21, 056318 (2014).
- [14] D. Kraus et al., *Phys. Plasmas* 25, 056313 (2018).
- [15] E. Bourasseau, N. Pineau, J. B. Mailliet, V. Dubois, *Carbon* 103, 464-472 (2016).
- [16] E. Garcia Saiz et al., *Nat. Phys.* 4, 940 (2008).
- [17] S.H. Glenzer and R. Redmer, *Rev. Mod. Phys.* 81, 1625 (2009).
- [18] T. Ma et al., *Phys. Rev. Lett.* 110, 065001 (2013).
- [19] D. Kraus et al., *Physics of Plasma* 22(5), 056307 (2015).
- [20] A. W. Moore, *Chemistry and physics of carbon: highly oriented pyrolytic graphite*, Marcel Dekker, New York, (1973).
- [21] G. Blaj, et al., *Journal of Synchrotron Radiation* 22, 577 (2015).
- [22] P. Eisenberger, and P. M. Platzman, *Phys. Rev. A* 2 415, (1970).
- [23] J. Chihara, *J. Phys. Condens. Matter* 12, 231 (2000).
- [24] J. Chihara, *J. Phys. F: Met. Phys.* 17, 295 (1987).
- [25] K. Wünsch, *Theory of X-ray Thomson Scattering in Warm Dense Matter*. PhD thesis. University of Warwick, (2011).
- [26] G. Gregori, S. H. Glenzer, W. Rozmus, R. W. Lee, and O. L. Landen, *Phys. Rev. E*, 67, 26412 (2003).
- [27] G. Gregori, S. H. Glenzer, F. J. Rogers, S. M. Pollaine, O. L. Landen, C. Blancard, G. Faussurier, P. Renaudin, S. Kuhlbrodt, and R. Redmer, *Phys. Plasmas* 11, 2754 (2004).
- [28] R. James, *The Optical Principles of the Diffraction of X-rays*, Ox Bow Press, London (1962).
- [29] L. Pauling and J. Sherman. *Zeitschrift für Kristallographie, Kristallgeometrie, Kristallphysik, Kristallchemie* 81, 1 (1931).
- [30] D. Kraus et al., *High Energy Density Physics* 8, 46 (2012).
- [31] J. Helfrich et al., *High Energy Density Physics*, 14, 38 (2015).
- [32] G. Kresse and J. Hafner. *Ab initio molecular dynamics for liquid metals*. *Phys. Rev. B*, 47, 558 (1993).
- [33] G. Kresse and J. Hafner. *Ab initio molecular-dynamics simulation of the liquid-metal-amorphous-semiconductor transition in germanium*. *Phys. Rev. B*, 49, 14251 (1994).
- [34] G. Kresse and J. Furthmüller. *Efficiency of ab-initio total energy calculations for metals and semiconductors using a plane-wave basis set*. *Comput. Mat. Sci.*, 6, 15 (1996).
- [35] G. Kresse and J. Furthmüller. *Efficient iterative schemes for ab initio total-energy calculations using a plane-wave basis set*. *Phys. Rev. B*, 54, 11169 (1996).
- [36] W.G. Hoover. *Canonical ensemble - equilibrium phase-space distributions* *Phys. Rev. A*, 31, 1695 (1985).
- [37] J. P. Perdew, K. Burke, and M. Ernzerhof. *Generalized gradient approximation made simple*. *Phys. Rev. Lett.*, 77, 3865 (1996).
- [38] J. P. Perdew, K. Burke, and M. Ernzerhof. *Erratum: Generalized gradient approximation made simple*. *Phys. Rev. Lett.*, 78, 1396 (1997).
- [39] P. E. Blochl. *Projector augmented-wave method*. *Phys. Rev. B*, 50, 17953 (1994).
- [40] G. Kresse and D. Joubert. *From ultrasoft pseudopotentials to the projector augmented-wave method*. *Phys. Rev. B*, 59, 1758 (1999).
- [41] J. Vorberger and D. O. Gericke, *High Energy Density Physics*, 9, 178 (2013).
- [42] L. B. Fletcher et al., *Nature Photonics* 9, 274279 (2015).
- [43] W. H. Gust, *Phys. Rev. B*, 22, 10, (1980).
- [44] M. van Thiel. *Compendium of shock wave data*. Lawrence Livermore Laboratory Report UCRL-50108 (1977).
- [45] W. J. Nellis, A. C. Mitchell, and A.K. McMahn, *Carbon at pressures in the range 0.1-1 TPA (10 MBar)*, *Journal of Applied Physics*, 90, 2 (2001).
- [46] S. P. Lyon und J. D. Johnson, *SESAME: The Los Alamos National Laboratory Equation of State Database*, LANL Report No. LA-UR-92-3407, 1992.
- [47] X. Wang et al., *Phys. Rev. Lett.* 95, 185701 (2005).
- [48] F. P. Bundy, W. A. Bassett, M. S. Weathers, R. J. Hemley, H. U. Mao und A. F. Goncharov, *Carbon* 34, 41 (1996).
- [49] A. A. Correa et al., *PNAS* 103, 1204 (2006).
- [50] M. P. Grumbach and R. M. Martin, *Solid State Communications* 100, 61 (1996).
- [51] M. van Thiel and F. H. Ree, *Phys. Rev. B* 48, 3591 (1992).
- [52] A. M. Molodets, *Free Energy of Diamond, Combustion, Explosion and Shock Waves* 34, 94 (1998).
- [53] L. E. Fried and W. M. Howard, *Phys. Rev. B*, 61, 8734, (2000).
- [54] L. M. Ghiringhelli, J. H. Los, E. J. Meijer, A. Fasolino and D. Frenkel, *Phys. Rev. Lett.* 94, 145701 (2005).